Dynamical Characterization of the Heme NO Oxygen Binding (HNOX) Domain. Insight into Soluble Guanylate Cyclase Allosteric Transition[†]

Luciana Capece,[‡] Dario A. Estrin,[‡] and Marcelo A. Marti*[,‡,§]

Departamento de Química Inorgánica, Analítica y Química Física/INQUIMAE-CONICET, and Departamento de Química Biológica, Facultad de Ciencias Exactas y Naturales, Universidad de Buenos Aires, Ciudad Universitaria, Pabellón 2, Buenos Aires, C1428EHA, Argentina

Received April 17, 2008; Revised Manuscript Received July 18, 2008

ABSTRACT: Since the discovery of soluble guanylate cyclase (sGC) as the mammalian receptor for nitric oxide (NO), numerous studies have been performed in order to understand how sGC transduces the NO signal. However, the structural basis of sGC activation is still not completely elucidated. Spectroscopic and kinetic studies showed that the key step in the activation mechanism was the NO-induced breaking of the iron proximal histidine bond in the so-called 6c-NO to 5c-NO transition. The main breakthrough in the understanding of sGC activation mechanism came, however, from the elucidation of crystal structures for two different prokaryotic heme NO oxygen (HNOX) domains, which are homologues to the sGC heme domain. In this work we present computer simulation results of *Thermoanaerobacter tencogensis* HNOX that complement these structural studies, yielding molecular explanations to several poorly understood properties of these proteins. Specifically, our results explain the differential ligand binding patterns of the HNOX domains according to the nature of proximal and distal residues. We also show that the natural dynamics of these proteins is intimately related with the proposed conformational dependent activation process, which involves mainly the αFβ1 loop and the αA−αC distal subdomain. The results from the sGC models also support this view and suggest a key role for the αFβ1 loop in the iron proximal histidine bond breaking process and, therefore, in the sGC activation mechanism.

Heme proteins, which are found in all living organisms (*1, 2*), are capable of performing a wide variety of tasks ranging from electron transport or oxidation of organic compounds, to the sensing and transport of small molecules, namely, O_2, CO, and NO.[1] All known sensor heme proteins belong to one of four structural groups. The first group is characterized by a myoglobin (Mb) like domain, as that contained in the HemAT aerotaxis regulating prokaryotic protein (*3*). The second group presents a PAS domain, found among others in the histidine kinase containing protein, Fix-L (*4*). The third group corresponds to the CO sensor CooA protein (*5*). The fourth group was the last to be structurally characterized and includes the heme domain of soluble guanylate cyclases (sGC) (*6*), the mammalian receptor for nitric oxide (NO) (*7, 8*).

sGC is a heterodimeric heme protein composed of α and β subunits. It is accepted that the ferrous heme is linked to the β-subunit via a histidine (His) residue (H105 in rat, human, and bovine sGC). A few years ago sequence analysis of the sGC heme domain allowed to identify several related prokaryotic domains (*9, 10*). These domains, which contain about 190 residues, are found in obligate anaerobes and facultative anaerobes. Several conserved residues are observed in the proximal and distal sites of the heme. As expected, His 102 is totally conserved as the proximal ligand, as are residues Tyr 131, Ser 133, and Arg 135, which conform to the Y-S-R motif involved in interaction with propionate moieties of the heme prosthetic group. Other conserved residues are Met 1, Gly 3, Gly 71, Pro 115, and Gly 143.

Further understanding of these domains came from the determination of the crystal structure of the oxygen binding HNOX domains from *Thermoanaerobacter tencogensis* (Tt-HNOX) (*11, 12*) and *Nostoc* sp. (Ns-HNOX) (*13*). The HNOX structure consists of seven α-helices (named A−G) and four stranded antiparallel β-sheets (named 1−4); the topology has no significant similarity with previously characterized protein folds (Figure 1). Domains from different bacteria characterized so far have shown the ability to bind NO, O_2, or both. Therefore, the name HNOX (for heme nitric oxide/oxygen binding domain) has been suggested for them (*11, 14−16*). The known structure of one HNOX domain prompted several studies about their ligand discrimination mechanism and their relation with the activa-

[†] This work was supported by grants of ANPCyT (National Science Agency of Argentina), CONICET, University of Buenos Aires, and by a fellowship of the J. S. Guggenheim Foundation to D.A.E.

* To whom correspondence should be addressed: tel, (5411)-45763380ext 105; fax, (5411)45763341; e-mail, marcelo@qi.fcen.uba.ar.

[‡] Departamento de Química Inorgánica.

[§] Departamento de Química Biológica.

[1] Abbreviations: sGC, soluble guanylate cyclase; NO, nitric oxide; HNOX, heme NO oxygen domain; Tt-HNOX, *Thermoanaerobacter tencogensis* HNOX protein; VCA, *Vibrio cholerae* HNOX protein; Ns-HNOX, *Nostoc* sp. HNOX domain; Mb, myoglobin; Hb, hemoglobin; Cyt *c′*, cytochrome *c′*; wt, wild type; Ct, carboxyl-terminal; Nt, amino-terminal; HB, hydrogen bond; 5c, five-coordinated; 6c, six-coordinated; MD, molecular dynamics; QM, quantum mechanical; QM/MM, hybrid quantum mechanical/molecular mechanics; MSMD, multiple steering molecular dynamics; IC, involvements coefficients; RMSD, root mean square deviation; RMSF, root mean square fluctuation.

10.1021/bi800682k CCC: $40.75
Published on Web 08/15/2008

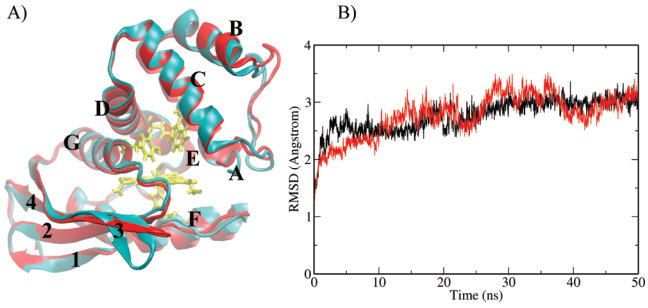

FIGURE 1: (A) Average structures of oxy (blue) and deoxy (red) Tt-HNOX structure showing the α-helix (A−G) and the β-sheet (1−4) labeling. (B) Backbone RMSD vs time plot for the oxy (black line) and deoxy (red line) Tt-HNOX 50 ns long MD simulation.

tion mechanism of sGC (*6*). One of the most relevant features of the Tt-HNOX structure is that it was crystallized in the oxygen-bound (oxy) state. The structure shows that distal Tyr 140 establishes a hydrogen bond (HB) interaction to the bound oxygen. The effect of this and other residues in the distal pocket was thoroughly investigated in relation with O_2 and NO discrimination in Tt-HNOX and also in several sGC constructs. However, the results are controversial. Mutation of Tyr 140 to an hydrophobic residue in Tt-HNOX increases 20-fold the O_2 dissociation rate (k_{off}) (*15*). The sGC contains a conserved Ile residue instead of Tyr in this position (Ile 145). In the same study Boon et al. showed that converting Ile 145 to Tyr in the sGC(1−385) heme domain fragment of sGC results in a protein that now is able to form a stable oxy complex, although the extremely low association rate constant indicates that is does not behave in the same way as the prokaryotic homologues (*15*). Moreover, the same Ile 145 Tyr mutant was introduced in full-length sGC, and the results showed no change in the ability of NO to activate the enzyme even in aerobic conditions and an inability to form a stable oxy complex (*17*). Another protein of this group is a 181 residue heme protein from *Vibrio cholerae* (VCA). This protein, in contrast to Tt-HNOX, is not able to bind O_2 similarly to sGC. VCA displays an apolar residue (A140) in the Tyr 140 position of Tt-HNOX (*16*). Another striking fact is that the HNOX domain of *Clostridium botulinum*, a strict anaerobe which displays the same distal residues than Tt-HNOX, is unable to form a stable oxy complex but has a remarkably stable NO complex (*11*). Moreover, the same authors found that Tt-HNOX is unable to form a stable oxy complex at the physiologically relevant temperature for this organism (70 °C) (*11*). Clearly, the mechanisms of ligand discrimination in the HNOX domains are far from understood.

Concerning the activation mechanism of sGC, also several questions remain unanswered. The main fact about the activation mechanism is that sGC becomes activated when NO binds to the heme group. The formation of a thermodynamically stable five-coordinated heme complex upon NO binding (5c-NO), with the associated Fe−His bond cleavage, is believed to be the trigger of a conformational change that activates the enzyme and transduces the NO signal (*6*). The ability of weakening the Fe−His bond (trans to the NO binding site) is a unique property of the NO ligand, as is called the NO negative trans effect (*18*). On the other hand, CO and O_2 display a positive trans effect; i.e., the Fe−His bond is strengthened upon ligand binding (*19*). Besides this fact, there is still a lot of debate about the precise role played by NO in the activation mechanism (*6*). Interestingly, while VCA forms (as well as sGC) 5c-NO complexes, Tt-HNOX remains 6c after NO binding (*16*).

In this work we present a theoretical study of Tt-HNOX structural dynamical and reactive characteristics using state of the art computer simulation techniques based on classical molecular dynamics (MD) and hybrid quantum chemical molecular mechanics (QM/MM) calculations. Simulations are performed for wild-type and mutant Tt-HNOX proteins and also for some sGC models. Our results show that the natural dynamics of the HNOX domain is intimately related with the proposed conformational dependent activation process, which involves mainly the αFβ1 loop and the αA−αC distal subdomain. The results also suggest a key role for the αFβ1 loop in the sGC activation mechanism. Last but not least, the differential ligand binding patterns toward O_2, CO, and NO of the HNOX domains are explained in a structural context.

COMPUTATIONAL METHODS

Setup of the System. (A) Initial Structures. We obtained initial structures of the oxy complex of the Tt-HNOX domain from the experimental X-ray determined structure by Pellicena et al. (PDB code 1U55). Other structures of this protein (PDB codes 1U4H, 1U56, (*12*) and 1XBN (*11*)) were used for comparison purposes. The starting unbound or deoxy Tt-HNOX structure was obtained by *in silico* removing the oxygen molecule from an equilibrated Tt-HNOX oxy structure.

Starting structures for the mutant Tt-HNOX protein and other HNOX protein models were obtained by performing the corresponding mutations *in silico* to the Tt-HNOX X-ray structure (*12*) using the Modeller software (*30*).

(B) System Setup and Equilibration. To set up the systems for the MD simulations, the starting structures were immersed in a preequilibrated octahedral box of TIP3P water molecules. The standard protonation state at physiological pH was assigned to the ionizable residues. All simulations were performed at 1 atm and 300 K, maintained with the Berendsen barostat and thermostat (*31*), using periodic boundary conditions and Ewald sums (grid spacing of 1 Å) for treating long-range electrostatic interactions with a 10 Å cutoff for computing direct interactions. The SHAKE algorithm was used to keep bonds involving H atoms at their equilibrium length, allowing to employ a 2 fs time step for the integration of Newton's equations. The Amber f99SB force field parameters (*32*) were used for all residues. The heme parameters in both coordination states used in this work were developed and thoroughly tested by our group in previous works (*20, 21, 33*). All simulations were performed with the SANDER module of the AMBER9 program (*34*).

Equilibration protocols consisted of performing an optimization of the initial structures, followed by a slow heating to the desired temperature. The equilibration is performed in two steps. First, a 500 ps constant volume MD run heats the system slowly to 300 K. Second, another 500 ps MD run at constant pressure is performed to achieve proper density. Once the system is equilibrated, the different production MD runs are performed. Frames were collected at 1 ps intervals, which were subsequently used to analyze the trajectories.

(C) Essential Dynamics. In order to get insight into the dynamical properties of each structure and their influence

on the structural transitions, several essential dynamics (ED) analyses were performed for all production MD runs (*35*). The ED for each run (or combination of runs) is determined by diagonalizing the covariance matrices (cov^T) of the atomic positions along the desired trajectory, obtaining the corresponding eigenvalues and eigenvectors (eq 1):

$$\mathrm{cov}^{\mathrm{T}} = \frac{1}{M}\sum_{k=1}^{M}\{[X_i(k) - \langle X_i\rangle][X_j - \langle X_j\rangle]\} \quad (1)$$

where the sum goes over the "M" configurations or snapshots from the dynamics, $X_i(k)$ corresponds to ith Cartesian coordinate of the system in snapshot number k, and $\langle X_i\rangle$ represents the mean value.

Each obtained eigenvector (ν_i) corresponds to an essential mode (EM) of the protein. Together, all of the essential modes describe the motion of the protein along the MD run used to generate the computed matrix. The eigenvalues (λ_i) obtained represent the relative contribution of each EM to the overall dynamics. The EM are ranked according their eigenvalues and therefore their relative weight, the first EM being the one with major contribution or larger eigenvalue. The ED were computed only for the backbone (N, C, Cα, O) atoms. Terminal residues were excluded since the high flexibility in this region might mask the essential movements of the protein's fold. In the first place, the EM for each individual MD run were computed and analyzed. Second, EM of combined trajectories (6c and 5c) were obtained to get a deeper insight into the structural transition.

Projections "$P_N(t)$" along the MD runs onto selected EM were also performed to analyze the configurational space explored along the MD run (eq 2):

$$P_N(t) = \nu_N r(t) \quad (2)$$

where ν_N is the EM number N and $r(t)$ is the protein conformation at time t. Projections are measured in angstroms, and the value corresponds to the overall deviation from the mean structure along the projected mode.

Comparison between different pairs of EM were performed using the similarity index (SI), which is the dot product between both the eigenvectors corresponding to two selected the EM (eq 3):

$$\mathrm{SI}_{AiBj} = \nu_{Ai}\cdot\nu_{Bj} \quad (3)$$

where Ai corresponds to EM number "i" of MD simulation "A". A value close to 1 means both modes are almost identical, whereas values close to zero indicate completely orthogonal or different modes. To have a global comparison of the dynamics for different protein states (A and B), a global SI (SI_{AB}) was computed as the sum of a desired number of SIs weighted by their eigenvalue and normalized by the total contribution of the compared modes to the overall dynamics (eq 4):

$$\mathrm{SI}_{\mathrm{AB}} = \frac{1}{\sum\lambda_i}\sum \mathrm{SI}_{AiBi}\cdot\lambda_i \quad (4)$$

where SI_{AB} in this case represents the similarity between MD A and B and λ_i is the average eigenvalue between the eigenvalues corresponding to ν_{Ai} and ν_{Ai} eigenvectors.

Based on the comparison of the equilibrium and transition EM, the involvement coefficients (IC) of each EM to a given structural transition were computed (eq 5) (*29*).

$$\mathrm{IC} = \nu_{Ai}\cdot V_{\mathrm{AB}}^{T} \quad (5)$$

In this case IC expresses how much of the structural transition between the vector representing the transition of structures A and B (V_{AB}^T) is contained in the EM number "i" of MD corresponding to a given state. This method therefore allows to analyze how much of the natural motions of the protein in a given state contribute to the selected conformational transition.

This type of analysis based on the essential dynamics has already proved useful in the study of the structural and dynamical relationships in several proteins (*36*−*40*), including the study of structural transitions (*28*).

QM-MM Calculations. QM-MM calculations were performed for the O_2-, NO-, and CO-bound protein complexes of wt Tt-HNOX and mutants. The initial structures for the QM-MM calculations were obtained from the MD runs in the oxy wt Tt-HNOX. The NO and CO complexes and the mutant proteins (resembling the VCA and SGC active sites) were constructed *in silico*. In these last cases, the systems were equilibrated by performing a 1 ns molecular dynamics run at 300 K. Selected snapshots for each structure were chosen and cooled slowly to 0 K. Starting from these frozen structures full hybrid QM-MM geometry optimizations of the oxygenated and deoxygenated proteins were performed using a conjugate gradient algorithm, at the DFT level with the SIESTA code using our own QM-MM implementation (*19, 20, 41*). For all atoms, basis sets of double plus polarization quality were employed, and all calculations were performed using the generalized gradient approximation functional proposed by Perdew, Burke, and Ernzerhof (*42*). Only residues located less than 10 Å apart from the heme reactive center were allowed to move freely in the QM-MM runs. The iron porphyrinate and the relevant ligands were selected as the quantum subsystem. The rest of the protein unit, together with water molecules, was treated classically. The interface between the QM and MM portions of the system was treated by the scaled position link atom method. The SIESTA code showed an excellent performance for medium and large systems and also proved to be appropriate for biomolecules and specifically for heme models. Further technical details about the QM-MM implementation can be found elsewhere (*19*−*21, 43, 44*).

O_2 binding energies (ΔE_{O_2}) were calculated as

$$\Delta E_{\mathrm{O2}} = E_{\mathrm{Prot\text{-}O2}} - (E_{\mathrm{O2}} + E_{\mathrm{Prot}}) \quad (6)$$

where $E_{\mathrm{Prot\text{-}O_2}}$ is the energy of the oxy protein, E_{prot} is the energy of the deoxy protein, and E_{O_2} is the energy of the isolated oxygen molecule.

Multiple Steering Molecular Dynamics. The multiple steering molecular dynamics (MSMD) approach, originally proposed by Jarzynski (*45*), is based on the following relation between the nonequilibrium dynamics and equilibrium properties:

$$\exp[-\Delta A(\xi)/k_{\mathrm{B}}T] = \langle \exp[-W(\xi)/k_{\mathrm{B}}T]\rangle \quad (7)$$

where $W(\xi)$ is the external work performed on the system as it evolves from the initial to the final state along the reaction coordinate ξ.

In MSMD the original potential is modified by adding to the potential energy a time-dependent external potential,

usually harmonic, that moves the system along the reaction coordinate by varying the potential well according to

$$E'(r) = E(r) + k[\xi - (\xi_0 + \nu\Delta t)]^2 \quad (8)$$

where ν is the pulling speed that moves the system along the reaction coordinate.

The PMF is obtained by performing several MSMD runs, collecting the work done at each time step and then properly averaging it, according to Jarzynski's equation (eq 7). Usually, the pulling speed is chosen so that the system moves smoothly but faster than in a true reversible simulation (*46*−*48*).

Free Energy Profiles of the 6c to 5c Transition. In order to get a thermodynamic picture of the 6c to 5c transition in all models, the corresponding free energy profiles were computed. The profiles were constructed by performing constant velocity multiple steered molecular dynamics (MSMD) as mentioned above. In the present study, the reaction coordinate was chosen as the Fe−His distance. Calculations were performed using a force constant of 200 kcal·mol^{-1}·Å^{-1} and pulling velocities of 3.75 × 10^{-3} and 7.5 × 10^{-3} Å/ps, both speeds yielded similar free energy profiles. Ten MSMD simulations were performed in each direction (forward/dissociation and backward/association), and the final profile is obtained by combining both. Since the reaction coordinate involves the formation/breaking of a bond (the Fe−His bond), a process not allowed in the standard MD force field, we introduced a Morse potential to describe the bond. The parameters in this case are an equilibrium distance of 2.01 Å and an energy constant of 10 kcal·mol^{-1}. The use of Morse potentials to study a reactive process in MD simulations has already been successfully employed in heme protein ligand binding studies (*49*). We used a value of 10 kcal/mol for the Fe−His bond dissociation energy. This value was chosen based on previous experience on the Fe−His dissociation process in other heme proteins (*21, 22, 28*).

RESULTS

The Results section is organized as follows. First, a structural and dynamical characterization of Tt-HNOX in the oxy and deoxy states is presented based on the 50 ns long classical MD simulations for each case. Second, a detailed study of wt and mutant Tt-HNOX active sites is performed for the O_2-, NO-, and CO-bound proteins using a hybrid QM-MM approach. Third, the 6c-NO to 5c-NO transition in Tt-HNOX is investigated by employing multiple steering MD (MSMD) methodology. Finally, the 6c to 5c transition is investigated in three loop models of sGC based on the Tt-HNOX structure.

Structural and Dynamical Comparison of Tt-HNOX in the Oxy and Deoxy States. (A) Stability of the Protein along the MD Simulation. We performed a 50 ns run for each protein state (oxy and deoxy). The average structure and the root mean square deviation (RMSD) vs time plot for both simulations is shown in panels A and B of Figure 1, respectively. As can be seen, oxy Tt-HNOX stabilizes in less than 5 ns, and the RMSD remains below 3Å, as expected, since the oxy Tt-HNOX was the starting structure. In the deoxy protein the final deviation is similar, but it is interesting to note that after the initial relaxation (of less than 1 ns) there is a continuous rise in the RMSD from 2 to 3 Å during the first 15 ns and that it presents low frequency variations.

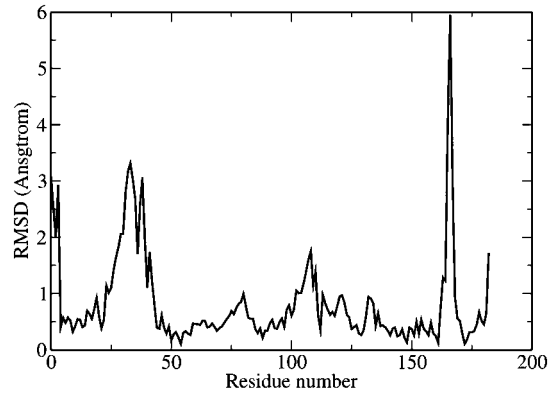

FIGURE 2: RMSD vs residue plot between oxy and deoxy Tt-HNOX average structures.

(B) Structural Characteristics of Tt-HNOX in the Oxy and Deoxy States. We start our comparison of the oxy and deoxy Tt-HNOX by comparing the average structures (computed for the last 45 ns of the MD run) of the oxy and deoxy Tt-HNOX. The overall RMSD between both structures is 1.12 Å considering only the backbone atoms, and it rises to 1.80 Å if all heavy atoms are considered. The same results are obtained if the average structure of deoxy Tt-HNOX is computed with only the last 30 ns of the MD runs. The RMSD for each residue between both average structures is shown in Figure 2.

As can be seen from Figures 1 and 2, and consistently with the low overall RMSD, both structures are very similar. Visual analysis indicates that the main differences are located at the end of the B α-helix and the BC loop (residues 24−42) which are displaced in the deoxy protein respect to the oxy protein upon overall alignment. This fact is evidenced by the fact that the RMSD for the rest of the protein is only 0.8 Å. Second, the $\beta3\beta4$ loop around residue 165 displays a different conformation in both structures (narrow peak in Figure 2). It is bent in the oxy protein (in blue) whereas in the deoxy protein it remains straight as shown in Figure 1. The third and smaller difference corresponds to a displacement of the proximal helix last residues along the helix axis and the residues corresponding to the αFβ1 loop.

(C) Dynamical Characterization of Tt-HNOX in the Oxy and Deoxy States. To analyze the protein dynamics, we computed the root mean square fluctuations (RMSF), which show the dispersion of each atomic position along the simulation, for both the oxy and deoxy MD simulations. The RMSF values are averaged for all atoms of each residue and plotted against residue number. The results from Figure 3 show that the fluctuations are similar in both cases with slightly larger fluctuations in the deoxy protein. The regions with higher mobility are the αFβ1 loop, the BC loop, and the $\beta3\beta4$ loop.

To analyze now Tt-HNOX dynamics in both coordination states, we performed an essential mode (EM) analysis based on both 50 ns MD runs. This method allows analyzing the whole dynamics as a small set of concerted movements represented by each EM. (See Table S1 in the Supporting Information for further information.) The nature of the collective motion for the two first EM for the oxy and deoxy proteins is shown in Figures 4 and 5 respectively. As shown

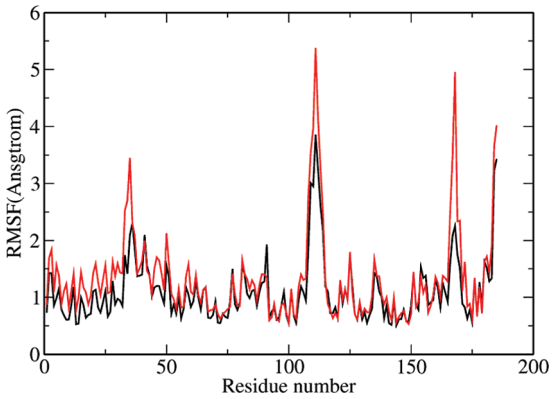

FIGURE 3: RMSF vs residue plot between oxy (black line) and deoxy (red line) Tt-HNOX MD simulations.

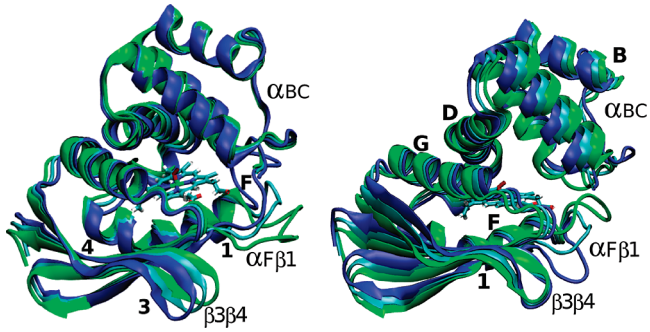

FIGURE 4: Structural movement for the first and second EM of the oxy Tt-HNOX. Helices are labeled in capital letters, and sheets are numbered.

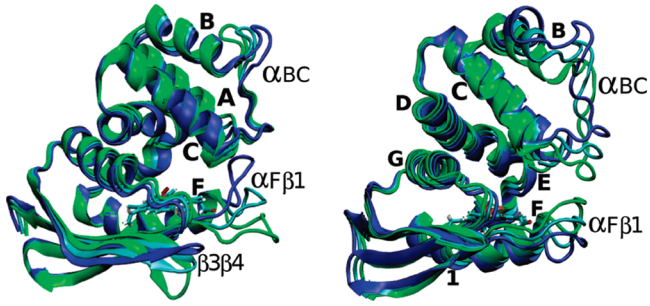

FIGURE 5: Structural movement for the first and second EM of the deoxy Tt-HNOX. Helices are labeled in capital letters, and sheets are numbered.

in Figure 4, in the oxy protein the first EM is localized mainly in the αFβ1 loop, with some contribution of the β3β4 loop. Both loops perform opposite flap movements resulting in the loops coming closer and further apart along the move. The second EM consists of collective motions of all the secondary structure groups. Using as fixed references the distal G-helix and proximal F-helix, the mode can be described as displacement of B and D helices against the G-helix Nt end. On the other hand, the four β-strands rotate together. There is also a significant contribution of αFβ1 loop movement along this mode.

In the deoxy protein, shown in Figure 5, the first EM is mainly localized in the Ct of the F-helix, the αFβ1 loop, and the β3β4 loop. Along this EM the αFβ1 and β3β4 loops move up and down together. There is also some contribution of an open−close movement of the αA-Nt and αD-Ct ends. The second EM consists of concerted movement of the B-helix and BC loop, plus the αF-Ct and αFβ1 loop. Along the mode (and opposite to EM1) the loops move closer and

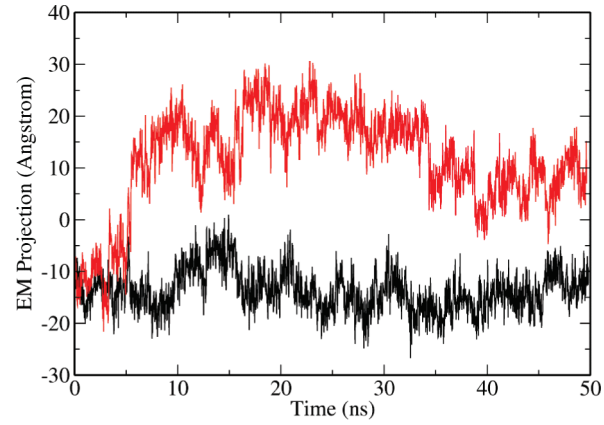

FIGURE 6: Projection of the oxy (black) and deoxy (red) MD simulations on the second EM computed for the MD and EM combined trajectory.

further. From a global view the mode can be described as a concerted movement of the distal αABC and proximal αFβ1−4 domains, using the αDE as a hinge region.

In both cases (oxy and deoxy) the other modes are more delocalized, showing small movements of several protein regions; however, they still display large contributions from the αBC, αFβ1, and β3β4 loops.

These results show that in both the oxy and deoxy proteins the first modes are located in the same region and are similar (62% similarity index). The second and third modes also show some similarity, with similarity values of 47% and 55%, respectively. The global similarity is 54%, meaning that roughly half of the structural variation is the same for both proteins, being located on the same regions.

(D) Characterization of the Oxy to Deoxy Transition by Combined EM Analysis. To get further insight into the differences between the oxy and deoxy species, we computed the EM combining both the oxy and deoxy MD simulations. This strategy allows analyzing the transition but including the information of the whole conformational space explored along both simulations. With this strategy usually the first or second EM is able to describe the transition between both conformational ensembles. In this case, the first EM computed by combining both trajectories, and which presents a 33% contribution to the overall structural variation, does not correspond to the transition but is similar to the first EM in both the oxy and deoxy MD simulations (≈90% similarity). This implies that this structural movement is of a similar magnitude than that of the oxy−deoxy transition, at least in the time scale of our simulation. On the other hand, the second mode (24% of the structural variation) clearly distinguishes both structures and represents the oxy to deoxy conformational transition.

The projection of this second EM along each run, presented in Figure 6, shows that while the oxy protein remains almost constant, the deoxy structure exhibits a transition of about 40 Å magnitude, remaining afterward in that conformation for the rest of the run. This indicates that the differential conformation between both states is maintained during the time scale of the simulation.

As expected, the transition from the oxy to deoxy species revealed by the combined EM analysis is consistent with the comparison of the average structures.

Table 1: Structural and Energetic Parameters of the Oxy Complexes of Several HNOX Domains[a]

	wt	Y140A	VCA	distal sGC
d Fe−O	1.81	1.78	1.83	1.86
d O−O	1.30	1.30	1.29	1.29
∠ Fe−O−O	117.0	122.5	118.0	122.3
d Fe−N_{im}	2.05	2.07	2.10	2.07
d Fe−N_{im} (deoxy)	2.11	2.11	2.18	2.13
qO_2	−0.346	−0.292	−0.248	−0.248
ΔE_{O_2}	33.3	28.2	28.6	28.2
k_{off}[b]	1.22	20.1	ND	ND

[a] Distances in angstroms, angles in degrees, energies in kcal/mol, charges in *e*, and k_{off} values in s^{-1}. d Fe−O, d O−O, and d Fe−N_{im} correspond to the corresponding bond distances in angstroms. ∠ Fe−O−O corresponds to the angle value in degrees. qO_2 corresponds to O_2 net Mulliken charge, ΔE_{O_2} corresponds to O_2 binding energy, and k_{off} corresponds to the experimentally observed O_2 kinetic dissociation constant. [b] See ref *15*.

Summing up, the results in this section show that both oxy and deoxy Tt-HNOX present the highest flexibility at the αFβ1 loop, the β3β4 loop, and the BC loop. The movement of the first two loops is represented in the first EM in both cases, while the movement of the BC loop is displayed in the second EM and plays a key role in the transition between both states.

Active Site Structure and Reactivity of Wild-Type and Mutant Tt-HNOX. To analyze the heme active site reactivity of Tt-HNOX, we performed QM-MM calculations for the O_2-, NO-, and CO-bound proteins, plus the 5c deoxy heme. For each case, we computed the optimized structure and selected thermodynamic parameters. For comparison purposes, mutants resembling the sGC or VCA active sites were also computed.

(A) Structure and Energetics of the Oxy Tt-HNOX Domains. We computed the oxy complexes of four proteins: wild type Tt-HNOX, Tyr 140 to Ala Tt-HNOX (Y140A), and a mutant resembling the distal cavity of sGC (distal-sGC) and of VCA. These last two distal models were built by performing the mutations I5V, W9L, N74F, F78C, and Y140I for the distal-sGC and mutations W9L, N74L, F78L, and Y140A for the VCA.

As mentioned in the introduction, the experimental fact is that neither sGC nor VCA binds oxygen whereas Tt-HNOX is able to form a stable oxy complex. Experimental studies showed that the most important residue in modulating affinity is Tyr 142. To study this issue, we have computed for the above-mentioned proteins the oxygen binding energy (ΔE_{O_2}). Previous results from our group for several heme proteins showed that ΔE_{O_2} shows good correlation with the oxygen release rate k_{off} (*20*). However, due to limitations in DFT description of the electronic structure, values are overestimated. The results for these calculations are shown in Table 1.

The results from Table 1 show that, as expected, the distal mutations have a significant impact on the oxygen complex structure and energetics. The wt Tt-HNOX has considerable binding energy consistently with the low k_{off} value. As expected, mutating the distal tyrosine reduces the binding energy and increases the dissociation rate (Figure 7A). Both sGC and VCA models that lack distal tyrosine (Figure 7B) have similar binding energy to the Y140A mutants. Also, in the mutant proteins the bound oxygen is less negatively charged, with a similar decrease in the negative charge of both oxygen atoms. The more negatively charged oxygen in wt Tt-HNOX increases the distal HB strength and thereby the oxygen affinity. The less negative charge on the oxygen in the other proteins may also represent a decrease in the π back-bonding from the iron which could lower the affinity. The last interesting point of these complexes is the *trans* effect reflected in the Fe−His distance. Oxygen is known to have a positive *trans* effect which is reflected in the strengthening of the Fe−His bond upon oxygen binding. This is shown in the structures as a shortening of the Fe−His bond upon oxygen binding. Interestingly, in both sGC and VCA protein models the Fe−His bond seems weaker than in wt and mutant Tt-HNOX, especially in the deoxy state, as reflected in longer bond lengths.

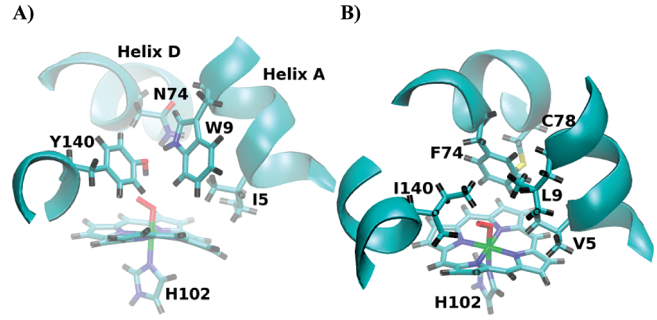

FIGURE 7: Active site structures of (A) oxy Tt-HNOX and (B) oxy sGC model.

Table 2: Structural Parameters of the NO Complexes Tt-HNOX, Cyt *c′*, Hbα, and Hbβ[a]

	Tt-HNOX	Cyt *c′*	Hbα	Hbβ
d Fe−N	1.72	1.74	1.77	1.76
d N−O	1.22	1.21	1.207	1.21
∠ Fe−N−O	136.0	136.9	136.2	137.5
d Fe−N_{im}	2.14	2.33	2.21	2.14
qNO	−0.153	−0.071	−0.070	−0.071
ΔqIm	0.120	0.080	0.115	0.16
*ν*Fe−His exp	218[b]	231[c]	207[d]	220[d]

[a] Distances in angstroms, angles in degrees, charges in *e*, and frequencies in cm^{-1}. d Fe−N, d N−O, and d Fe−N_{im} correspond to the corresponding bond distances in angstroms. ∠ Fe−N−O corresponds to the angle value in degrees. ΔqIm and qNO correspond to the proximal imidazole and NO net Mulliken charges, respectively, and *ν*Fe−His exp corresponds to the experimental Fe−His stretching frequency. [b] See ref *16*. [c] See ref *23*. [d] See ref *24*.

(B) Structure of the NO-Bound Tt-HNOX Domains. In order to get some insight into the possible activation mechanism of sGC and VCA, we computed the structure of the NO complexes of wt Tt-HNOX. The results together with the results for Cyt *c′* and for the α and β hemoglobin chains (Hbα and Hbβ) (from our previous work) (*21, 22*) are shown in Table 2.

Key to sGC activation by NO is the NO *trans* effect that weakens and finally breaks the proximal Fe−His bond. We have shown previously that in order to break the Fe−His bond a weak bond is required and that the strength is modulated in part by the charge transfer from the histidine to the iron, as modulated by the hydrogen bond interactions through the Hδ with the rest of the protein (*22*). Proteins with neutral histidines such as Cyt *c′*, a protein which has shown to share spectroscopic and ligand binding characteristics similar to sGC (*21*) and Hbα among others, form a 5c-NO complex with the proximal histidine bond broken, whereas other proteins such as the Hbβ chain have strongly

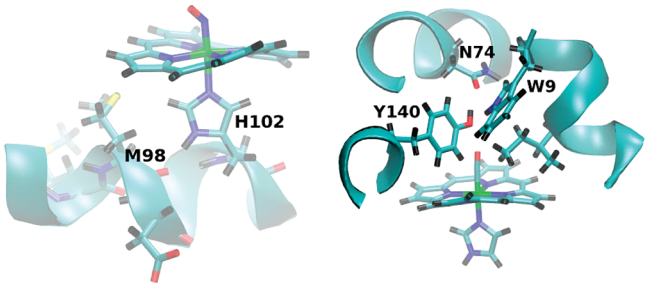

FIGURE 8: Active site structures of (A) NO-bound Tt-HNOX and (B) CO-bound Tt-HNOX.

bound histidines and form 6c-NO complexes (*21, 22*). As can be seen from Table 2, the proximal histidine of Tt-HNOX in the NO complex has similar characteristics to Hbβ (short Fe−His bond and more than 0.1 *e* charge transfer), a fact that is consistent with forming a stable 6c-NO complex. Figure 8A shows the proximal site structure of Tt-HNOX. In both proteins, Tt-HNOX and Hbβ, the proximal histidine is H-bonded to a carbonyl group from the protein backbone, which is Met 98 in Tt-HNOX. This H-bond probably contributes to strengthen the Fe−His bond. It should be noted, however, that the presence of an H-bond to the proximal histidine alone does not ensure a strong Fe−His bond, since steric strain may weaken it as is the case for Hbα (*22*).

(C) Structure and Vibrational Frequencies of the CO-Bound Tt-HNOX Domains. CO has been extensively used as an electrostatic probe for the polarity of the distal cavities in heme proteins. Due to its strong Stark effect it is very sensitive to the distal interactions when bound to the heme. In the Fe−CO moiety, the excess electron density on the iron is donated to the π^* orbital of the CO (π back-bonding). In this context, the Fe−CO is described by the following two resonance structures (Scheme 1).

Scheme 1

$$\underset{\text{I}}{\text{Fe}^{\delta-}-\text{C}\equiv\text{O}^{\delta+}} \leftrightarrow \underset{\text{II}}{\text{Fe}=\text{C}=\text{O}^{\delta-}}$$

As a general rule, stabilization of structure II, with an increase in the Fe−CO bond order and a decrease in the CO bond order, is reflected in lower CO stretching (νCO) and higher Fe−C stretching (νFe−C) frequency values. Consequently, when νFe−C is plotted against νCO, many heme proteins fall on a single line with negative slope reflective of the back-bonding (*25, 26*). The extent of back-bonding is controlled among other factors by the electrostatic environment in the distal pocket. Distal HB donor groups enhance back-bonding, lowering νFeC and increasing νCO. The νFeC/νCO data for sGC indicate a weak back-bonding, but the reason for this fact is not totally clear. Moreover, Tt-HNOX and VCA show significant deviations from the νFeC/νCO correlation with high νCO values, but higher than expected from the νFeC values. We computed the structure and CO frequency of the CO-bound wild-type Tt-HNOX and both the sGC and VCA distal models. Interestingly, during the preparative 1 ns MD simulation for wt Tt-HNOX, two possible conformations of the distal pocket were found in the CO complex. Conformation 1 (cf1) has the same hydrogen bond pattern as that observed for the oxy complex, i.e., with the Tyr 140 forming an HB with the bound CO (Figure 7A). On the other hand, in the second conformation (cf2), shown in Figure 8B, the Tyr 140 phenolic OH is pointing away from the bound CO and forms a hydrogen bond with the carbonyl of the Asn 74 side chain. The results are shown in Table 3.

Table 3: Structural Parameters of the CO Complexes of HNOX Domains[a]

	Tt-HNOX cf1	Tt-HNOX cf2	VCA	sGC
d Fe−C	1.724	1.758	1.756	1.774
d C−O	1.182	1.175	1.178	1.176
∠ Fe−C−O	176.0	176.0	177.0	174.2
d Fe−N_{im}	2.04	2.05	2.07	2.06
qC	0.006	0.002	0.00	−0.01
qO	−0.077	0.016	0.005	0.016
qCO	−0.071	0.018	0.005	0.015
νCO	1918	1968	1933	1943
νCO exp[b]	1989		1985	1987
νFe−C exp[b]	490		491	472

[a] Distances in angstroms, angles in degrees, charges in *e*, and frequencies in cm^{-1}. d Fe−C, d C−O, and d Fe−N_{im} correspond to the corresponding bond distances in angstroms. ∠ Fe−C−O corresponds to the angle value in degrees. qC, qO, and qCO correspond to the carbon atom, oxygen atom, and net CO Mulliken charges. νCO, νCO exp, and νFe−C exp correspond to the computed or experimental (exp) stretching frequency values. [b] See ref *16*.

The results from Table 3 show that as expected the computed νCO is related to the amount of back-bonding; the less back-bonding (more positive CO) the higher the computed frequency. The results show that the three structures (Tt-HNOX cf2, sGC, and VCA) which show a slightly positive CO display also larger Fe−C and smaller CO distances compared to Tt-HNOX cf1. Consistently, with these values the computed frequencies for Tt-HNOX cf2, sGC, and VCA are higher than for Tt-HNOX cf1, although the computed value for VCA is lower than expected from its structural properties. It should be noted that the computed frequencies are less accurate than the distances and qCO values. In this context the experimental νCO frequency values appear to be consistent with the three Tt-HNOX cf2, sGC, and VCA structures but not with Tt-HNOX cf1. As mentioned above for these proteins a weak back-bonding effect is expected from νCO data consistent with our structures. A possible source for the weaker back-bonding in HNOX domains is the strong HB to the heme propionates as suggested by Xu et al. (*25*) In the same work it was suggested that Tt-HNOX and VCA deviations from the νFeC/νCO correlation, due to a higher than expected νFe−C, could arise from a compression of the Fe−C bond. Our results are also consistent with this hypothesis since both in Tt-HNOX (cf1 and cf2) and VCA the Fe−C bond is shorter than that of sGC which displays a lower νFeC.

In conjunction, the structures for the three ligands remark the importance of Tyr 140 in ligand binding. In addition, the results for NO binding show a high Fe−His bond strength, consistently with a stable 6c-NO complex. In the following section, the 6c to 5c transition is analyzed for the Tt-HNOX and three sGC models.

Hexacoordinated to Pentacoordinated Transition in Tt-HNOX. It has been reported that the iron−histidine bond in Tt-HNOX is not broken upon NO binding, and our QM-MM data confirm this is unlikely to happen in part due to a too strong Fe−His bond. However, the 6c-NO to 5c-NO transition is supposed to be the trigger of the conformational

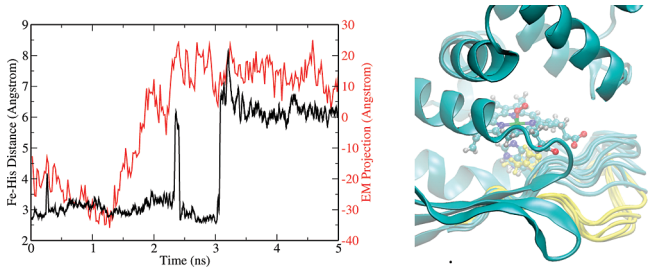

FIGURE 9: (A, left) Black line: Fe−His distance vs time plot for the histidine unbound MD simulation of Tt-HNOX. Red line: First His unbound EM projection on the His unbound MD simulation. (B, right) Change in αFβ1 loop due to 6c to 5c transition. Histidine and the loop conformation in the 5c state are depicted in yellow. Histidine and the loop conformation in the 6c state are depicted in light blue. The heme group is also shown.

change that results in sGC activation. For these reasons, and in order to get possible insights into sGC activation mechanism, we decided to study by means of MD simulations the 6c to 5c transition in Tt-HNOX.

First, we performed a MD simulation where the Fe−His bond was artificially severed (called from now on His unbound MD run). Figure 9A shows the Fe−His distance along the simulation. As can be seen from this figure, the histidine remains close to the iron (similar to the 6c conformation) for 3 ns, except for a fast swing movement at 2.4 ns corresponding to the spike observed in the black trace of Figure 9, and then abruptly completely detaches from the heme adopting a completely unbound conformation (5c conformation). This transition is characterized by a rotational movement along the Cα−Cβ bond of the histidine, as characterized by the C−Cα−Cβ−Cγ dihedral angle which changes from values around 160° (6c state) to about 40° (5c state). In the 6c state the His Hδ is H-bonded to the Met 98 carbonyl whereas in the 5c state it is H-bonded to the Pro 166 carbonyl. The most important change due to the 6c to 5c transition is observed in the αFβ1 loop as shown in Figure 9B. When the histidine detaches from the heme, the αFβ1 loop moves down further from the distal domain.

To further characterize the 6c to 5c transition, observed in the unbound MD simulation, we computed the EM for this short run. As expected, the first EM (which contributes to 50% of the overall mobility) correlates with the transition and is, as expected from the data mentioned above, located in the αFβ1 loop. Figure 9A (red line) shows the projection of this EM onto the MD simulation. It is interesting to note that before the histidine can detach the global transition must happen, and once finished, histidine changes conformation. The overall transition is relatively slow and requires ≈1 ns to occur. Interestingly, in the spike histidine detaches from the heme, but since the αFβ1 loop transition is not complete, it rebinds to the heme, further supporting the connection of these two events.

αFβ1 Loop Models of sGC. To analyze the possible structure and characteristics of the αFβ1 loop of sGC, which according to the above-mentioned results is an important region in the dynamics of the HNOX domain, and particularly concerning proximal histidine, we built an αFβ1 loop model of sGC based on the Tt-HNOX structure. The model was built replacing residues 95 to 118 in the Tt-HNOX residue sequence for the corresponding sequence of residues in sGC, as shown in the sequence alignment in Table 4. The sequence of the sGC model is based on the multiple alignments of HNOX domains (*12*). One hundred different possible loop conformations were built with the Modeler program (as explained in the Computational Methods section) and ranked by energy. The nine models with the lowest overall potential energy and the model based on the Tt-HNOX loop structure were clustered according to their loop RMSD values; models with RMSD of less than 2 Å were considered together. From this analysis, five models were selected and subjected to a MD relaxing protocol in implicit solvent. After relaxing the five models were again compared on an RMSD basis, and finally three models (M1, M2, and M3) were selected and subjected to 8 ns MD simulation in explicit water. The resulting secondary structure classification of the loop residues according to the ϕ/ψ angles for each model is shown in Table 4.

The difference between Tt-HNOX and the sGC model structures is in residues M95 to L118. As expected, initial replaced residues continue to display helical structure corresponding to Ct of αF, and the last correspond to a β-sheet secondary structure of β1.

Figure 10 shows the average structure obtained for the last 5 ns of each simulation, in conjunction with the Tt-HNOX structure. During the whole simulation, the conformation of the αFβ1 loop was maintained, although the αFβ1 loop was shown to be the region with the highest fluctuations. (See Figure S1 in Supporting Information.)

To provide further insight into the 6c to 5c transition from a thermodynamic viewpoint, we computed the free energy profile of His release in Tt-HNOX and in the three sGC selected models. We simulated the Fe−His bond with a Morse potential (as mentioned in the Computational Methods section). Although we could use a QM/MM scheme to describe the Fe−His bond and the concomitant ligation dependent structural transition as studied by Alcantara et al. (*27*), the computational cost of our QM/MM scheme is too high to allow obtaining the free energy profile associated with the coordination. In addition, the use of the Morse potential has already been successfully applied to study Fe−His coordination dependent conformational changes in previous works (*28*). Given that the Fe−His bond energy value is the same for all models and also for Tt-HNOX, they should be interpreted from a comparative view and not a quantitative accurate measure of the free energy difference between 6c and 5c structures.

The free energy profiles for the 6c to 5c process are shown in Figure 11. Interestingly, the three sGC models displayed a lower barrier than the Tt-HNOX for the 6c to 5c transition, remarking the importance of the αFβ1 loop in the process. For Tt-HNOX the 6c to 5c barrier is of 12.5 kcal/mol, bigger than the 10 kcal/mol expected solely from the energy needed to break the Fe−His bond, meaning that in Tt-HNOX the loop structure disfavors the 6c to 5c transition. On the other hand, for the M2 and M3 sGC models the barrier is 10 kcal/mol and for M1 it is even lower. These results suggest than in sGC the loop favors the 6c to 5c transition. Moreover, for M2 also a shallow minimum for the 5c is observed showing stabilization of these states in the model.

DISCUSSION

Since the discovery of sGC as the mammalian receptor for NO, numerous studies have been performed in order to

Table 4: Sequence and Secondary Structure (SS) for the αFβ1 Loop in Tt-HNOX and the Three Selected sGC Models

Tt-HNOX	residue	M	M	M	D	E	V	H	L	Q	L	T	K	M	I	K	G	A	T	P	P	R	L
	SS	α	-	α	α	α	α	α	α	α	α	α	α	α	-	L	-	β	β	β	β	β	β
sGC models	residue	Q	N	L	D	A	L	H	D	H	L	A	T	I	Y	P	G	M	R	A	P	S	F
M1	SS	-	β	α	α	α	α	α	α	α	-	-	-	α	β	β	-	L	-	β	β	β	β
M2		-	-	α	α	α	α	α	α	α	-	β	β	β	β	β	-	β	β	α	β	β	β
M3		-	-	α	α	α	α	α	α	α	-	β	β	-	β	β	-	L	-	β	α	β	β

understand how sGC transduces the NO signal. However, probably due to the lack of crystal structures no detailed structural mechanism of how NO actives sGC has been proposed. Spectroscopic and kinetic studies showed that the key step in the activation mechanism was the breaking of the Fe−His bond *trans* to the NO, the so-called 6c-NO to 5c-NO transition, once the NO was bound (*6*). CO, which is only able to form a 6c-CO complex, only activates sGC weakly. The main breakthrough in the understanding of the sGC activation mechanism came from crystallization of the prokaryotic HNOX domains (*12, 13*), which are homologue to the sGC heme domain. Our work, based on the structure of the Tt-HNOX domain, complements these structural studies yielding molecular explanations to several poorly understood properties of these proteins and new dynamical information about how these proteins work.

As already mentioned in the introduction, Tt-HNOX and sGC have different reactivity patterns toward both O_2 and NO. Tt-HNOX binds O_2 with moderate affinity whereas sGC is unable to bind it, and previous studies showed that the main responsible of this effect was the presence of Tyr 140 in the Tt-HNOX distal cavity that stabilized the bound O_2 through HB interactions. Our results for the QM-MM of wt and Y140A mutant Tt-HNOX calculations are consistent with these data. In the sGC and VCA distal models no HB donor residues are observed in the distal cavity and therefore, and consistently with experimental observations, the oxygen binding affinity is lower compared to Tt-HNOX. Our results also suggest that the high CO stretching frequency observed for Tt-HNOX, similar to that of sGC and VCA, may arise in part from an alternative conformation of Tyr140-OH which is H bonded to Asn 74 and not to CO.

Another interesting point about Tt-HNOX is its inability to form a 5c-NO complex remaining in the 6c-NO state with an intact Fe−His bond. Our QM/MM results show that the Fe−His bond seems too strong to be broken due to the non-neutral characteristic of the proximal histidine. The nonneutral characteristic of the proximal histidine arises probably as a consequence of the HB between the Hα and the Met 98 carbonyl. The MD results of the 6c to 5c transition, however, show that if the bond were weaker, a stable 5c-

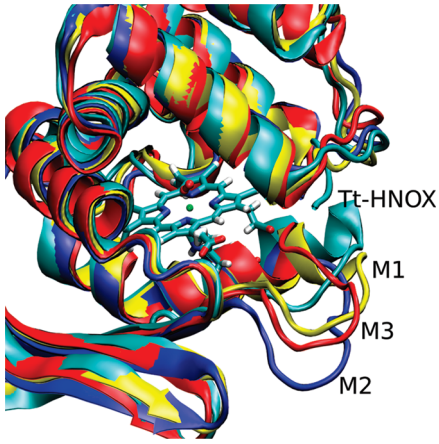

FIGURE 10: Average structures obtained from the MD simulations of M1, M2, and M3 sGC models. Tt-HNOX average structure is shown for comparative purposes.

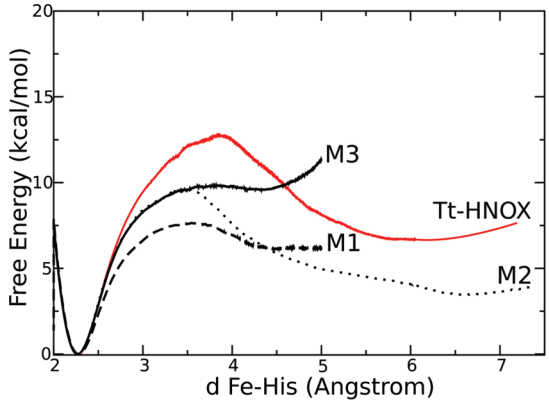

FIGURE 11: Free energy profiles for Tt-HNOX (red), M3 (black), M2 (black dotted), and M1 (black dashed) sGC models.

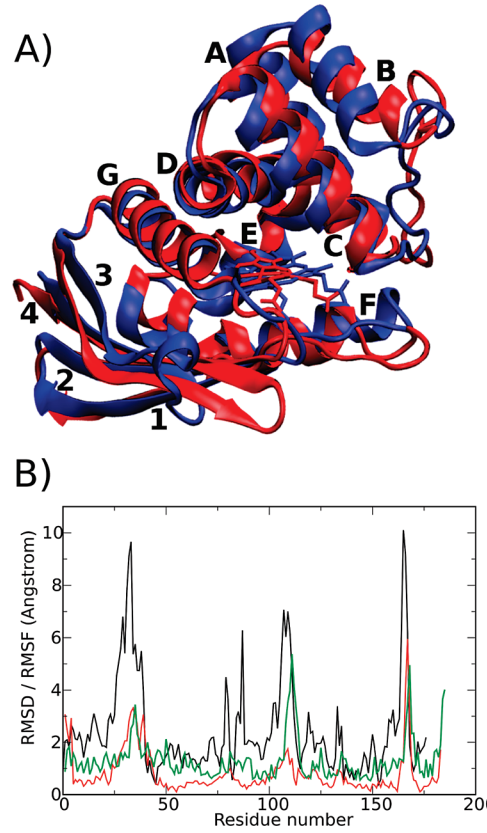

FIGURE 12: (A) Structural comparison of oxy Tt-HNOX and deoxy Ns-HNOX X-ray structures (*13*). (B) RMSD vs residue plot between oxy Tt-HNOX and deoxy Ns-HNOX X-ray structures (black line), RMSD vs residue plot between oxy and deoxy Tt-HNOX average structures (red line), and the oxy Tt-HNOX RMSF vs residue plot (green line).

Table 5: Involvement Coefficients (IC) of the Equilibrium EM (Eq EM) for Oxy and Deoxy Tt-HNOX and the Combined 6c to 5c EM of Tt-HNOX and the Three sGC Models to the Transition Described by the Oxy Tt-HNOX and Ns-HNOX Structures

	Tt-HNOX Eq EM		5c to 6c transition EM			
mode no.	deoxy	oxy	Tt-HNOX	M1	M2	M3
1	−0.185	0.352	−0.21	−0.06	0.23	0.17
2	−0.21	0.097	−0.08	−0.19	−0.07	0.15
3	−0.098	0.065	−0.31	−0.06	0.04	0.26
4	−0.034	0.058	0.011	−0.06	0.1	0
5	0.062	−0.032	−0.11	0.03	−0.03	0.09
accumulated	0.59	0.61	0.72	0.4	0.47	0.67

NO conformation exists, with the histidine rotated around the Cα−Cβ bond. Moreover, the results show that this transition must be preceded by a conformational rearrangement of the αFβ1 loop and that in Tt-HNOX the loop structure also disfavors the 5c to 6c transition.

From a more global viewpoint, insight into the NO-mediated sGC allosteric activation mechanism came from the comparison of the different HNOX crystal structures (*12, 13*). Based on the oxy Tt-HNOX and the deoxy, NO- and CO-bound Ns-HNOX a structural activation model was proposed (*13*). In this model the oxy Tt-HNOX represents the fully activated state and the deoxy and CO/NO Ns-HNOX represent the basal and low activity structures. The main observed structural transitions are a displacement of the αA−αC distal subdomain which comes closer to the heme during activation, an increase in the disorder and temperature factors of the αFβ1 loop, (Figure 12A), and a pivot-bend displacement of the heme (*13*).

In order to relate the proposed activation model with the results obtained in this work, we performed two comparisons. First, we calculated the involvement coefficients (IC) (see Computational Methods), which relate the transition described by the "activated" Tt-HNOX crystal structure and the "inactivated" deoxy Ns-HNOX, with the EM obtained from the Tt-HNOX oxy and deoxy equilibrium MD simulations and the combined MD simulations describing the 6c to 5c in Tt-HNOX and the three sGC models. The IC coefficients measure the relation between the transition described by the two selected structures and the EM from a given MD simulation. Values close to zero mean no relation between the motion described by the EM and the structural transition, whereas values between 0.1 and 0.5 may be expected for an EM which is indeed related to the transition (*29*). The results for the computed IC are shown in Table 5. Second, we computed the residue displacements between Tt-HNOX and Ns-HNOX structures for direct comparison with Figures 2 and 3; the results are shown in Figure 12A).

The results from Figure 12B show that the difference in the oxy and deoxy Tt-HNOX average structures is localized in the same regions as the structural difference between Tt-HNOX and Ns-HNOX structures. The differences obtained for the X-ray structures are, however, of a larger magnitude, which is not surprising since they correspond to different homologue proteins and not the same protein in two states. Figure 12B also shows that the fluctuations of Tt-HNOX along the MD simulations are localized in the regions that undergo the proposed conformational change.

In addition, Ma et al. (*13*) remarked the role of residues W74 and M144 in Ns-HNOX, since they are involved in steric contacts with the helix A and the heme D propionate group, respectively. In Tt-HNOX residue 74 (Trp in Ns-HNOX) corresponds to a much smaller residue Asn 74 and therefore is not involved in steric contact with helix A. Residue 144 (Met in Ns-HNOX) corresponds to Tyr 140 and is not interacting with the CAD atom of the heme propionate group (as proposed for Ns-HNOX) since it is the tyrosine involved in hydrogen bond with the bound oxygen. In this context, no significant effect on the conformational change is expected for these two residues in Tt-HNOX.

The results for the IC shown in Table 5 also support the idea that the conformational space explored by Tt-HNOX along the equilibrium MD and those related with the 6c to 5c transition are related to the proposed activation conformational change, since the accumulated IC values are between 0.59 and 0.72. Specifically, the first EM for the oxy protein, which displays a significant IC of 0.352, is related to the structural transitions located in the αFβ1 loop and β3β4 loop. A lower contribution to the activation transition is shown by the second EM of the oxy protein (see Figures 12A and 4 for a visual comparison). In the deoxy protein the highest IC of 0.21 is displayed by the second EM which describes the activation conformational motion of the distal Nt domain (compare Figure 5B with Figure 12A).

Finally, the IC obtained for the EM of the 6c and 5c combined trajectories for the sGC models show that the conformational change of the transition characterized by the proximal histidine detachment and the concomitant αFβ1 loop structural change is related in part to the proposed activation mechanism. Indeed, the first EM for the combined trajectories, which describes most of the transition, has significant IC values (except for M1 where the second EM mode has the highest IC).

Taken together, these results suggest that the conformational space explored by the Tt-HNOX along the dynamics and in the oxy/deoxy transition and the 6c to 5c transition are similar to that observed for the different crystal structures proposed to reflect the activation mechanism and that although ligand binding characteristics are different between Tt-HNOX and Ns-HNOX, a common structural transition between the inactive and active forms can be expected.

Concerning the sGC activation mechanism, although in Tt-HNOX the Fe−His bond is not broken in the NO complex, our results revealed that the αFβ1 loop movement is tightly coupled to histidine displacement if the Fe−His bond breaks. Given the relation between the conformational change of the αFβ1 loop and the proposed activation mechanism based on the Tt-HNOX and Ns-HNOX crystal structures, the results for the 6c to 5c transition yield significant information on the activation mechanism. Our results show that for Tt-HNOX the αFβ1 loop opposes to the 6c to 5c transition whereas in the sGC models the transition is slightly favored. These data are consistent with

the experimental facts which show that sGC but not Tt-HNOX is able to form a stable 5c complex and suggest that the αFβ1 loop may have a key role in sGC activation.

CONCLUSION

Our results show that the differential ligand binding patterns toward O_2, CO, and NO of the HNOX domains can be explained in relation with the proximal and distal residues present in each protein. We also proved, based on an essential dynamics analysis of oxy and deoxy Tt-HNOX, that the natural dynamics of the protein are intimately related with the proposed conformational dependent activation process, which involves mainly the αFβ1 loop and the αA−αC distal subdomain. The results from the sGC models also support this view and suggest a key role for the αFβ1 loop in the iron proximal histidine breaking process and, therefore, in the sGC activation mechanism.

SUPPORTING INFORMATION AVAILABLE

RMSF vs residue for M1, M2, and M3 sGC models and essential mode (EM) contribution in percentage to the overall protein dynamics along the MD simulation of Tt-HNOX. This material is available free of charge via the Internet at http://pubs.acs.org.

REFERENCES

1. Kadish, K. M., Smith, K. M. , and Guilard, R. (2000) *The porphrin handbook*, *Vol. 4*, Academic Press, San Diego.
2. Lecomte, J. T. J., Vuletich, D. A., and Lesk, A. M. (2005) Structural divergence and distant relationships in proteins: Evolution of the globins. *Curr. Opin. Struct. Biol. 15*, 290–301.
3. Hou, S., Larsen, R. W., Boudko, D., Riley, C. W., Karatan, E., Zimmer, M., Ordal, G. W., and Alam, M. (2000) Myoglobin-like aerotaxis transducers in Archaea and Bacteria. *Nature 403*, 540–544.
4. Gilles-Gonzalez, M. A., Ditta, G. S., and Helinski, D. R. (1991) A haemoprotein with kinase activity encoded by the oxygen sensor of Rhizobium meliloti. *Nature 350*, 170–172.
5. Roberts, G. P., Kerby, R. L., Youn, H., and Conrad, M. (2005) CooA, a paradigm for gas sensing regulatory proteins. *J. Inorg. Biochem. 99*, 280–292.
6. Poulos, T. L. (2006) Soluble guanylate cyclase. *Curr. Opin. Struct. Biol. 16*, 736–743.
7. Denninger, J. W., and Marletta, M. A. (1999) Guanylate cyclase and the •NO/cGMP signaling pathway. *Biochim. Biophys. Acta 1411*, 334–350.
8. Moncada, S., Palmer, R. M. J., and Higgs, E. A. (1991) Nitric oxide: Physiology, pathophysiology, and pharmacology. *Pharmacol. Rev. 43*, 109–142.
9. Iyer, L. M., Anantharaman, V., and Aravind, L. (2003) Ancient conserved domains shared by animal soluble guanylyl cyclases and bacterial signaling proteins. *BMC Genomics 4*.
10. Schmidt, P. M., Schramm, M., Schroder, H., Wunder, F., and Stasch, J. P. (2004) Identification of residues crucially involved in the binding of the heme moiety of soluble guanylate cyclase. *J. Biol. Chem. 279*, 3025–3032.
11. Nioche, P., Berka, V., Vipond, J., Minton, N., Tsai, A. L., and Raman, C. S. (2004) Femtomolar sensitivity of a NO sensor from Clostridium botulinum. *Science 306*, 1550–1553.
12. Pellicena, P., Karow, D. S., Boon, E. M., Marletta, M. A., and Kuriyan, J. (2004) Crystal structure of an oxygen-binding heme domain related to soluble guanylate cyclases. *Proc. Natl. Acad. Sci. U.S.A. 101*, 12854–12859.
13. Ma, X., Sayed, N., Beuve, A., and van den Akker, F. (2007) NO and CO differentially activate soluble guanylyl cyclase via a heme pivot-bend mechanism. *EMBO J. 26*, 578–588.
14. Karow, D. S., Pan, D., Davis, J. H., Behrends, S., Mathies, R. A., and Marletta, M. A. (2005) Characterization of functional heme domains from soluble guanylate cyclase. *Biochemistry 44*, 16266–16274.
15. Boon, E. M., Huang, S. H., and Marletta, M. A. (2005) A molecular basis for NO selectivity in soluble guanylate cyclase. *Nat. Chem. Biol. 1*, 53–59.
16. Karow, D. S., Pan, D., Tran, R., Pellicena, P., Presley, A., Mathies, R. A., and Marletta, M. A. (2004) Spectroscopic characterization of the soluble guanylate cyclase-like heme domains from Vibrio cholerae and Thermoanaerobacter tengcongensis. *Biochemistry 43*, 10203–10211.
17. Rothkegel, C., Schmidt, P. M., Stoll, F., Schroder, H., Schmidt, H. H. H. W., and Stasch, J. P. (2006) Identification of residues crucially involved in soluble guanylate cyclase activation. *FEBS Lett. 580*, 4205–4213.
18. Scheidt, W. R., and Ellison, M. K. (1999) The synthetic and structural chemistry of heme derivatives with nitric oxide ligands. *Acc. Chem. Res. 32*, 350–359.
19. Bikiel, D. E., Boechi, L., Capece, L., Crespo, A., De Biase, P. M., Di Lella, S., Gonzalez Lebrero, M. C., Marti, M. A., Nadra, A. D., Perissinotti, L. L., Scherlis, D. A., and Estrin, D. A. (2006) Modeling heme proteins using atomistic simulations. *Phys. Chem. Chem. Phys. 8*, 5611–5628.
20. Marti, M. A., Crespo, A., Capece, L., Boechi, L., Bikiel, D. E., Scherlis, D. A., and Estrin, D. A. (2006) Dioxygen affinity in heme proteins investigated by computer simulation. *J. Inorg. Biochem. 100*, 761–70.
21. Marti, M. A., Capece, L., Crespo, A., Doctorovich, F., and Estrin, D. A. (2005) Nitric oxide interaction with cytochrome c′ and its relevance to guanylate cyclase. Why does the iron histidine bond break? *J. Am. Chem. Soc. 127*, 7721–7728.
22. Marti, M. A., Scherlis, D. A., Doctorovich, F. A., Ordejon, P., and Estrin, D. A. (2003) Modulation of the NO trans effect in heme proteins: implications for the activation of soluble guanylate cyclase. *J. Biol. Inorg. Chem. 8*, 595–600.
23. Andrew, C. R., G, S. J., Lawson, D. M., and Eady, R. R. (2001) Resonance Raman studies of cytochrome c′ support the binding of NO and CO to opposite sides of the heme: Implications for ligand discrimination in heme-based sensors. *Biochemistry 40*, 4115–4122.
24. Schelvis, J. P., M. S, S. A., Cerda, J. F., Garavito, R. M., and Babcock, G. T. (2000) Interaction of nitric oxide with prostaglandin endoperoxide H synthase-1: Implications for Fe-His bond cleavage in heme proteins. *J. Phys. Chem. B 104*, 10844–10850.
25. Xu, C., Ibrahim, M., and Spiro, T. G. (2008) DFT analysis of axial and equatorial effects on heme-CO vibrational modes: Applications to CooA and H-NOX heme sensor proteins. *Biochemistry 47*, 2379–2387.
26. Phillips, G. N., Jr., Teodora, M. L., Li, T., Smith, B., and Olson, J. S. (1999) Bound CO is a molecular probe of electrostatic potential in the distal pocket of myoglobin. *J. Phys. Chem. B 103*, 8817–8829.
27. Alcantara, R. E., Xu, C., Spiro, T. G., and Guallar, V. (2007) A quantum-chemical picture of hemoglobin affinity. *Proc. Natl. Acad. Sci. U.S.A. 104*, 18451–18455.
28. Nadra, A. D., Martí, M. A., Pesce, A., Bolognesi, M., and Estrin, D. A. (2008) Exploring the molecular basis of heme coordination in human neuroglobin. *Proteins: Struct., Funct., Bioinf. 71*, 695–705.
29. Tama, F., and Sanejouand, Y. H. (2001) Conformational change of proteins arising from normal mode calculations. *Protein Eng. 14*, 1–6.
30. Fiser, A., and Sali, A. (2003) MODELLER: Generation and refinement of homology-based protein structure models. *Methods Enzymol. 374*, 461–491.
31. Berendsen, H. J. C., Postma, J. P. M., Van Gunsteren, W. F., DiNola, A., and Haak, J. R. (1984) Molecular dynamics with coupling to an external bath. *J. Chem. Phys. 81*, 3684–3690.
32. Hornak, V., Abel, R., Okur, A., Strockbine, B., Roitberg, A., and Simmerling, C. (2006) Comparison of multiple amber force fields and development of improved protein backbone parameters. *Proteins: Struct., Funct., Genet. 65*, 712–725.
33. Bidon-Chanal, A., Marti, M. A., Crespo, A., Milani, M., Orozco, M., Bolognesi, M., Luque, F. J., and Estrin, D. A. (2006) Ligand-induced dynamical regulation of NO conversion in Mycobacterium tuberculosis truncated hemoglobin-N. *Proteins. Struct., Funct,. Bioinf.*
34. Pearlman, D. A., Case, D. A., Caldwell, J. W., Ross, W. S., Cheatham Iii, T. E., DeBolt, S., Ferguson, D., Seibel, G., and Kollman, P. (1995) AMBER, a package of computer programs for applying molecular mechanics, normal mode analysis, molecular

dynamics and free energy calculations to simulate the structural and energetic properties of molecules. *Comput. Phys. Commun. 91*, 1–41.
35. Amadei, A., Linssen, A. B. M., and Berendsen, H. J. C. (1993) Essential dynamics of proteins. *Proteins. Struct. Func. Gen. 17*, 412–425.
36. Amadei, A., Ceruso, M. A., and Di Nola, A. (1999) On the convergence of the conformational coordinates basis set obtained by the essential dynamics analysis of proteins' molecular dynamics simulations. *Proteins: Struct., Funct., Genet. 36*.
37. Amadei, A., De Groot, B. L., Ceruso, M. A., Paci, M., Di Nola, A., and Berendsen, H. J. C. (1999) A kinetic model for the internal motions of proteins: Diffusion between multiple harmonic wells. *Proteins: Struct., Funct., Genet. 35*.
38. Chau, P. L., Van Aalten, D. M. F., Bywater, R. P., and Findlay, J. B. C. Functional concerted motions in the bovine serum retinol-binding protein. *J. Comput.-Aided Mol. Des. 13*.
39. De Groot, B. L., Vriend, G., and Berendsen, H. J. C. (1999) Conformational changes in the chaperonin GroEL: New insights into the allosteric mechanism. *J. Mol. Biol. 286*.
40. Kitao, A., and Go, N. (1999) Investigating protein dynamics in collective coordinate space. *Curr. Opin. Struct. Biol. 9*.
41. Crespo, A., Scherlis, D. A., Marti, M. A., Ordejón, P., Roitberg, A. E., and Estrin, D. A. (2003) A DFT-based QM-MM approach designed for the treatment of large molecular systems: Application to chorismate mutase. *J. Phys. Chem. B 107*, 13728–13736.
42. Perdew, J. P., Burke, K., and Ernzerhof, M. (1996) Generalized gradient approximation made simple. *Phys. Rev. Lett. 77*, 3865–3868.
43. Marti, M. A., Crespo, A., Bari, S. E., Doctorovich, F. A., and Estrin, D. A. (2004) QM-MM study of nitrite reduction by nitrite reductase of Pseudomonas aeruginosa. *J. Phys. Chem. B 108*, 18073–18080.
44. Crespo, A., Marti, M. A., Kalko, S. G., Morreale, A., Orozco, M., Gelpi, J. L., Luque, F. J., and Estrin, D. A. (2005) Theoretical study of the truncated hemoglobin HbN: Exploring the molecular basis of the NO detoxification mechanism. *J. Am. Chem. Soc. 127*, 4433–4444.
45. Jarzynski, C. (1997) Nonequilibrium equality for free energy differences. *Phys. Rev. Lett. 78*, 2690–2693.
46. Hummer, G., and Szabo, A. (2001) Free energy reconstruction from nonequilibrium single-molecule pulling experiments. *Proc. Natl. Acad. Sci. U.S.A. 98*, 3658–3661.
47. Park, S., and Schulten, K. (2004) Calculating potentials of mean force from steered molecular dynamics simulations. *J. Chem. Phys. 120*, 5946–5961.
48. Xiong, H., Crespo, A., Marti, M., Estrin, D., and Roitberg, A. E. (2006) Free energy calculations with non-equilibrium methods: Applications of the Jarzynski relationship. *Theor. Chem. Acc. 116*, 338–346.
49. Meuwly, M., Becker, O. M., Stote, R., and Karplus, M. (2002) NO rebinding to myoglobin: A reactive molecular dynamics study. *Biophys. Chem. 98*.

BI800682K